# Superresolution imaging of live samples by centroid reassignment microscopy

Chuan Li[1, 3, *], Quan Le[2], Julian O. Kimura[4, 5], Bingying Zhao[1, 3], Yunzhe Li[6], Jian Zhao[4, 5], Thomas Bifano[3], Brandon Weissbourd[4, 5], John T. Ngo[2], Jerome Mertz[2,3, *]

[1]Department of Electrical & Computer Engineering, Boston University, Boston, MA 02215, USA

[2]Department of Biomedical Engineering, Boston University, Boston, MA 02215, USA

[3]Photonics Center, Boston University, Boston, MA 02215, USA

[4]Department of Biology, MIT, Cambridge, MA 02139, USA

[5]The Picower Institute for Learning and Memory, MIT, Cambridge, MA 02139, USA

[6]Department of Electrical Engineering and Computer Sciences, UC Berkeley, Berkeley, CA 94720, USA

*e-mail: chuanli1@bu.edu; jmertz@bu.edu

## ABSTRACT

Superresolution imaging has become one of the most important recent advances in microscopy development. However, most superresolution methods are ill-adapted for live-sample imaging because they are unacceptably slow, susceptible to artifacts, or require the use of specialized fluorophores and labeling protocols. We introduce a superresolution method called centroid reassignment microscopy (CRM) that overcomes these limitations. CRM is a simple variation on confocal microscopy wherein the single-element detector and small pinhole are replaced by a centroid detector and larger pinhole. Superresolution is obtained by reassigning the centroid location of the detected fluorescence as a function of the scanning excitation focus location. Our method bears resemblance to the method of image scanning microscopy, which involves the use of an array detector, with the advantage that CRM provides improved resolution for the same number of detected photons while being simpler to implement. CRM is light-efficient, fast (single frame), robust to defocus aberrations, and requires no changes whatsoever in standard fluorescence imaging protocols, making it uniquely attractive for superresolution imaging of live, dynamic samples.

## INTRODUCTION

High-resolution optical imaging is essential for uncovering the dynamic architecture of living biological systems, including mitochondrial fission and fusion[1,2], axonal transport[3,4], synaptic plasticity[5,6], cytoskeletal remodeling[7,8], etc.. Capturing such events requires imaging approaches that not only deliver high spatial resolution beyond the diffraction limit (< 200 nm) but also maintain long-term sample viability[9]. While several superresolution approaches have been applied to live-sample imaging[9], these have been hindered by significant challenges. Single-molecule localization microscopy (SMLM) approaches [10–17] (such as Photoactivated Localization Microscopy (PALM) and STochastic Optical Reconstruction Microscopy (STORM)) require the use of specialized blinking or photoswitchable molecules, often requiring hundreds or thousands of raw images and restrictive sample preparation protocols. Stimulated-emission depletion (STED) approaches [18] require complex instrumentation involving high illumination powers, with a limited range of fluorophore compatibility. While structured illumination approaches overcome many of these issues, they too suffer from their own drawbacks. Structured illumination microscopy [19,20] (SIM) based on frequency multiplexing, requires an accurate estimation of the illumination patterns, making it susceptible to noise and aberrations. Random illumination microscopy [21] (RIM), which requires hundreds of raw image acquisitions, is susceptible to motion artifacts. To date, superresolution microscopy approaches have come nowhere close to the broad range of applicably for live-sample imaging as traditional confocal microscopy.

Indeed, traditional confocal microscopy can itself be considered a structured illumination approach [22], though with limited superresolution capacity. To obtain the best resolution from a confocal microscope, its pinhole must be closed to zero size, which is not possible in practice, thus imposing a compromise between resolution and signal strength. This compromise has been resolved by image scanning microscopy [22,23] (ISM), which provides essentially the same resolution of as a closed-pinhole confocal, but with the light collection efficiency of an open pinhole. ISM involves replacing the single-element detector of a confocal microscope with an array detector, allowing the possibility of superresolution by pixel reassignment. Initial incarnations of ISM involved computational reassignment [22,23], with speeds limited by both acquisition and computation times, though made faster with the advent of the Zeiss AiryScan [24]. It was later discovered that ISM could also be achieved all-optically [25,26], and generalized to

multi-point scanning [27,28]. Optical reassignment techniques have the advantage of directly providing superresolved images without the need for calculations, however, they lack the versatility and flexibility of computational approaches. For example, they cannot on the fly compensate for differences between excitation and emission PSFs, or PSF distortions induced by local aberrations, etc.. More recently, the advent of SPAD array detectors has reignited an interest in computational ISM [29,30]. These are small arrays of detectors, typically 5×5 in size [31], that respond at GHz rates, enabling much faster imaging than conventional camera-based approaches, even extending ISM to fluorescence lifetime imaging applications[29,30,32,33]. However, as small as a 5×5 array size appears, it imposes the acquisition of 25 signals through 25 independent electronic channels with high bandwidth and low noise, quickly making the electronics of ISM unwieldy.

We introduce an alternative approach to obtaining superresolution imaging while maintaining high light collection efficiency. The crux of our approach involves replacing the array detector of an ISM with a centroid detector which, at any given time, reports only the total intensity incident on the detector and its 2D centroid location. That is, it reports almost an order of magnitude reduced data compared to array detectors conventionally used for ISM. Our technique, called Centroid Reassignment Microscopy (CRM), is a simple variation on conventional confocal microscopy that is entirely compatible with conventional (non-blinking) fluorophores. CRM combines the benefits of centroid localization, associated with localization-based superresolution approaches [11,12], and pixel reassignment, associated with ISM. Compared to ISM, CRM provides resolution that surpasses the closed-pinhole limit (we demonstrate here sub-100 nm resolution), while being simpler to implement and less susceptible to detector noise. In addition, CRM automatically corrects for local aberrations and/or mismatches between excitation and emission PSF sizes without user intervention, enabling the possibility of extended depth of field (EDOF) imaging. In short, CRM is a uniquely attractive and versatile alternative to current superresolution approaches specifically designed for live sample imaging, as we demonstrate below.

# RESULTS

## Principle

To gain an understanding how CRM works, one must consider the principles of scanning fluorescence microscopy in general (see Fig. 1a). Conventionally, a single laser-beam focus is scanned in two dimensions in the sample, producing a scanning excitation spot centered at $\boldsymbol{\rho}_{ex} = \{x_{ex}, y_{ex}\}$ with intensity profile given by the excitation PSF. The resultant fluorescence is then de-scanned through the same scanning mechanism. We consider here the general case where the fluorescence is detected by an array detector conjugate to the sample plane (in the presence of an open or closed pinhole). The coordinates of the array detector elements are given by $\boldsymbol{\rho}_d$. That is, at any given time, a detector element at $\boldsymbol{\rho}_d$ captures fluorescence emission from a spot in the sample plane centered at $\boldsymbol{\rho}_{em} = \boldsymbol{\rho}_d - \boldsymbol{\rho}_{ex}$ with a detection efficiency profile given by the emission PSF. Both $\boldsymbol{\rho}_{ex}$ and $\boldsymbol{\rho}_{em}$ are implicitly time dependent by virtue of scanning, and the resultant intensity captured by the array detector is given by $I(\boldsymbol{\rho}_{ex}, \boldsymbol{\rho}_{em})$. Note that this intensity distribution is 4-dimensional. To construct a 2D image from this 4D distribution, different options are available (for simplicity we assume equal excitation and emission point spread functions – more general cases are considered in the Supplementary Notes). If the pinhole is open and $I(\boldsymbol{\rho}_{ex}, \boldsymbol{\rho}_{em})$ is projected over $\boldsymbol{\rho}_{ex}$ , corresponding to a pooling over all $\boldsymbol{\rho}_{ex}$ values, this leads to a widefield image $I_{wide}(\boldsymbol{\rho}_{em})$ (Fig. 1b). Similarly, if it is projected over $\boldsymbol{\rho}_{em}$, corresponding to a pooling of the detector pixels, this also leads to a widefield image $I_{wide}(\boldsymbol{\rho}_{ex})$ (Fig. 1b). Both widefield images are equivalent by reciprocity [34], and both yield modest spatial resolution. Improved resolution is obtained by closing the pinhole and performing confocal detection. In this case, a confocal image $I_{conf0}(\boldsymbol{\rho}_{ex})$ is constructed from only the diagonal elements $I(\boldsymbol{\rho}_{ex}, \boldsymbol{\rho}_{em} = \boldsymbol{\rho}_{ex})$ (yellow diagonal). However, because of the spatial filtering introduced by the pinhole, such detection produces only weak signal with poor SNR. In practice, the pinhole must be opened somewhat, leading to an image $I_{conf}(\boldsymbol{\rho}_{ex})$ with compromised resolution. This compromise can be circumvented by performing ISM, that is, by opening the pinhole and instead performing a projection of $I(\boldsymbol{\rho}_{ex}, \boldsymbol{\rho}_{em})$ along the anti-diagonal direction. As is apparent in Fig. 1b, $I(\boldsymbol{\rho}_{ex}, \boldsymbol{\rho}_{em})$ is most sparse along this direction, and a pair of point objects can be better resolved. Importantly, because ISM requires no spatial filtering, no power is lost in

principle, and high SNR is maintained. However, as noted above, ISM can be burdensome to implement and provides only modest resolution gain.

CRM, which involves replacing the array detector in Fig. 1a with a centroid detector, is yet an alternative approach for obtaining high resolution while maintaining high SNR. As noted above, CRM can be thought of as combining the benefits of localization and pixel reassignment. In conventional localization-based superresolution strategies, such as PALM/STORM, the location of a fluorophore is determined from the centroid of its emission distribution [11,12]. Said differently, the emission centroid provides a maximum-likelihood estimate of the fluorophore location. However, this is only true when no additional a priori knowledge is available, such as when the excitation intensity is spread uniformly across the field of view (the case for most PALM/STORM implementations). If instead the excitation is structured, additional information becomes available and the emission centroid no longer necessarily provides the maximum-likelihood estimate of the fluorophore location. For the case here where the excitation intensity is focused, the fluorophore is most likely located between the emission and excitation centroids (at the midpoint for equal PSFs). For the emission centroid to correspond to the fluorophore location, it must therefore be reassigned accordingly. This principle of reassignment is similar to that used by ISM, with the difference that CRM performs centroid reassignment, whereas ISM performs individual pixel reassignment. Our setup is described in detail in Methods. In Supplementary Note 1, we show that a centroid measurement followed by reassignment is equivalent to pixel reassignment followed by a centroid measurement. The benefit of the former is that it requires only a centroid detector rather than a full array detector.

Of course, while a centroid measurement can localize an individual fluorophore, it is not sufficient, by itself, to resolve the presence of multiple fluorophores in close proximity. For example, the emission centroid of two nearby fluorophores imaged by a conventional widefield microscope (e.g. gray traces from Fig. 1b) would lie at the midpoint between the fluorophores. The spatial separation of the fluorophores is not sufficient in this case to isolate their PSFs. What is needed is an additional dimension to enhance this separation. For PALM/STORM, this additional dimension is time, as assured by the use of blinking fluorophores. For CRM, it is also time, but assured instead by the use of beam scanning (CRM does not require blinking

molecules). That is, because of scanning, the two fluorophores appear not only at slightly different spatial locations, but also at slightly different times. CRM exploits this temporal gain in sparsity. As can be observed in Fig. 1c, the centroid location $\widehat{\boldsymbol{\rho}}_{em}$ (cyan trace) associated with two nearby fluorophores is no longer fixed at the midpoint between the fluorophores but rather jogs over time from one fluorophore to the next, clearly highlighting their separation. CRM involves reassigning the total power measured by the centroid detector and reassigning this power to a location situated between $\widehat{\boldsymbol{\rho}}_{em}$ and $\boldsymbol{\rho}_{ex}$. The reassigned powers are then accumulated over the total scan duration (i.e. over all $\boldsymbol{\rho}_{ex}$ values), resulting in a final CRM image. We note that different weights can be associated with $\widehat{\boldsymbol{\rho}}_{em}$ and $\boldsymbol{\rho}_{ex}$ when calculating the reassignment location $\boldsymbol{\rho}_r$. As detailed in Supplementary Notes 3, reassigning $\boldsymbol{\rho}_r$ to a location roughly midway between $\widehat{\boldsymbol{\rho}}_{em}$ and $\boldsymbol{\rho}_{ex}$ (reassignment factor $\alpha \approx 1/2$) leads to smoother images with higher fidelity and is more suitable when the fluorescence labeling is dense. On the other hand, reassigning $\boldsymbol{\rho}_r$ closer to $\widehat{\boldsymbol{\rho}}_{em}$ ($\alpha \approx 1$) yields sharper features and is more suitable when the fluorescence labeling is sparse.

**CRM image formation and reconstruction**

The only hardware differences between a CRM and a conventional confocal microscope are that we make use of a largely opened pinhole and a centroid detector. Different types of centroid detectors are available. Here, to achieve sufficient bandwidth, we make use of a simple quadrant detector (QD – see Methods). However, by itself, a QD cannot report centroid location. An additional scaling factor is needed related to the spot size incident on the QD. This scaling factor can be estimated a priori based on the known magnification and resolution of the optics. Alternatively, it can be measured experimentally using a strategy of image cross-correlation introduced in [35] and later used in [29]. Different from previously, we measure the scaling factor locally rather than globally, as discussed in Methods. The scaling factor $\vec{s}$ is thus adjusted throughout the image to account for local aberrations, etc..

In Fig. 2, we provide a schematic of our CRM algorithm based on the use of a QD as a centroid detector (more details provided in Methods). We imaged anti-α-tubulin labeled microtubules in the fixed Bovine Pulmonary Artery Endothelial Cells. Fig. 2c-e illustrates the resolution improvement provided by CRM compared to conventional confocal microscopy (summed four

quadrants), allowing two microtubules separated by about 175 nm to be much better distinguished. A now standard method of evaluating microscope resolution, particularly suitable for superresolution imaging, is the method of Fourier Ring Correlation (FRC) [36]. Based on a FRC analysis (Fig. 2f), the resolution provided by CRM for this example is 121 nm (reassignment factor $\alpha = 0.7$).

**Effect of reassignment factor on CRM**

The degree of spatial resolution achieved by reassignment microscopes depends on their reassignment factor $\alpha$. To demonstrate this, we compare CRM with a state-of-the-art commercial ISM (Zeiss LSM980 Airyscan2 -- see Methods) with sequential two-color imaging of fixed BPAE cells (Fig. 3a: F-actin in green, mitochondria in magenta). For proper comparison, the illumination powers, pixel sizes and pixel dwell times were set to be equal. The effect of different reassignment factors on resolution was evaluated by the method of FRC. As expected, CRM and ISM provide similar resolution for $\alpha = 0$, namely that of conventional confocal microscopy. For ISM, the best resolution is obtained for $\alpha \approx 1/2$. In contrast, for CRM the resolution continues to increase with increasing $\alpha$, leading to improved separability of features when $\alpha \to 1$. This is in qualitative agreement with our expectations from theory and simulation (Supplementary Note 3). We note that the size of the individual detector elements in the Airyscan was 0.2 Airy units (AU), limiting the overall ISM resolution, whereas CRM is not subject to this limitation. Based on our FRC analysis (Fig. 3c), we found that when using a 1.42 NA oil-immersion objective (Olympus, UPlanXApo 60x/1.42 Oil), CRM could provide a resolution as fine as 90 nm. In Extended Data Fig. 1, we further confirm these results by imaging 100 nm fluorescent beads. The measured separation between two beads in close proximity, as inferred from their peak locations, does not change with different values of $\alpha$, demonstrating a large degree of flexibility in the choice of the reassignment factor for CRM.

**CRM resolution improvement is robust to noise**

Major advantages of CRM are its high light collection efficiency and improved resolution capacity compared to ISM for equal photon budget. In Fig. 4, we provide an overview of the effect of different illumination powers (hence different SNR levels) on image resolution. Note

that from the same Airyscan raw data we can synthesize a standard confocal image (summation of all detector pixels), a small-pinhole confocal image (only central detector pixel), and an ISM image (reassigned detector pixels). These are compared with images obtained with CRM, again with equal illumination powers, pixel size and pixel dwell times. To reduce variations in our FRC analysis induced by background, aberrations or signal level, we averaged our FRC results over 8 distinct regions in Fig. 4a. Again, CRM provides the highest resolution. An advantage of the FRC method is that it takes into account the detrimental effects of detection noise (shot noise, electronic noise, etc.) on resolution. We observe that the resolution enhancement provided by CRM becomes all the more significant at lower excitation powers where a reduced SNR more severely undermines image quality (particularly apparent in the case of the small-pinhole confocal). The above results were obtained using a reassignment factor $\alpha = 0.8$, which was chosen to provide a balance between resolution enhancement and image fidelity. The resilience of CRM to noise is further validated in Supplementary Fig. 8, which provides simulations of line-pair imaging as a function of detected photon counts. Because CRM provides better resolution than ISM for equal photon budget, the same number of detected photons becomes compressed into smaller areas, leading to consistently improved SNR in the evaluation of line separability. Note that for these simulations, we included only shot noise. Had we also included detector noise, the improved performance of CRM would have been further accentuated owing to its reduced number of detector elements.

**Live sample imaging of CRM**

CRM is highly light-efficient, making it well suited for long-term imaging of live samples. In Fig. 5, we provide examples of live-sample imaging of dynamic processes such as mitochondrial fission and fusion in U2OS osteosarcoma cells and neuronal motion in jellyfish. For the U2OS experiments (Fig. 5a-b), we recorded a 10-minute time-lapse video of a single U2OS cell using gated illumination (see Methods). CRM is able to resolve morphological dynamics in U2OS mitochondria more effectively than standard confocal microscopy (summation of four quadrants), enabling us to more clearly observe mitochondria fusion events (Fig. 5b and Supplementary Video 2) and fission events (Extended Data Fig. 2 and Supplementary Video 3) over time scales consistent with previous reports[1,2]. Note that the integrated preamplifier in our QD limited our maximum pixel rate to about 2 MHz, which nevertheless allowed us to attain

video-rate (30 Hz) imaging speeds for frames as large as 256×256 pixels (Supplementary Video 4). For live jellyfish imaging, we used continuous illumination. As is apparent from the extracted frames (Fig. 5c-d) and full videos (Supplementary Video 5 & 6), CRM enables much finer features to be resolved in the motion dynamics of two neuronal bodies. In addition to increasing spatial resolution, CRM also increases signal-to-background ratio (SBR), as also shown in the Extended Data Fig. 4. The reason for this is that signal structure becomes reassigned by CRM into smaller areas, while background, which is mostly uniform, produces no centroid displacement and thus remains largely untouched.

**CRM enables EDOF imaging**

In practice, it is often preferable to operate CRM with a pinhole that is somewhat closed so as to benefit from a degree of optical sectioning dependent on pinhole size. In the event that the pinhole is largely open, the optical sectioning becomes weak, meaning that out-of-focus signal becomes incident on the QD. In effect, this leads to a broadening of the emission PSF, and hence to an increase in the scaling factor $\vec{s}$ required for centroid calculation. Inasmuch as our estimation of $\vec{s}$ is based on quadrant image cross-correlation (see Methods), CRM is able to adaptively adjust for such PSF broadening. Moreover, since the estimations are performed locally, the reassignment scaling factors can vary across the sample. If parts of the sample are more out of focus than others, CRM adaptively adjusts for this. As a result, CRM enables clear visualization of fine structures even when the sample exhibits depth variations. This is shown in Extended Data Fig. 3, where the out-of-focus blurring apparent in the confocal images is largely compensated for by CRM, here across a depth range of 10 μm. That is, CRM is robust to defocus aberrations, enabling the possibility of extended depth of field (EDOF) imaging. More broadly, though not demonstrated here, CRM is expected to be robust to more general aberrations than defocus, provided these do not cause an overall shifting of the centroid of the emission PSF.

## DISCUSSION

Different metrics can be used to characterize the resolution of a microscope [36], in either the Fourier domain (e.g. the Abbe limit) or the pixel domain (e.g. the Rayleigh limit). The former is often readily apparent when viewing the intensity spectra of images, as illustrated in Fig. 2c. The

latter, which characterizes the separability of two emitters, is generally more relevant for biological imaging since organelles of interest tend to be localized. We have shown that CRM provides better emitter separability than both confocal microscopy and ISM. Compared to a confocal microscope, CRM is similarly simple and can be implemented as an add-on with minimal modifications to any conventional confocal microscope, provided the latter is equipped with 4-channel electronics. The main benefit of CRM is that it maintains full detection efficiency since it does not require the use of a closed pinhole. This benefit preserves SNR even when imaging at low light levels, such as encountered when imaging at high speed or with reduced excitation powers, as often imposed with live-sample imaging. Compared to ISM, CRM makes use of fewer detectors, simplifying the detection electronics and mitigating electronic noise, all while providing sharper images for equal photon budget.

However, CRM does not come without drawbacks. The main drawback is that it is nonlinear, meaning that the CRM imaging process cannot be described as a convolution with a PSF. The degree of nonlinearly increases with the reassignment parameter $\alpha$. On the one hand, it is precisely this nonlinearity that facilitates emitter separability and leads to sharper images than ISM. On the other hand, when image linearity is a concern, it may be necessary to decrease $\alpha$ to the point where CRM and ISM images become similar. Another drawback of CRM (also shared by ISM) is that, because it avoids the use of a pinhole, it sacrifices the main benefit that comes from a pinhole, namely, a capacity for optical sectioning. In practice, we have found that CRM works best in combination with a pinhole that is not fully opened, thus benefiting from some degree of optical sectioning without undue sacrifice of detection efficiency. The presence of a pinhole has the additional effect of smoothing the CRM images (as does a reduction in $\alpha$). Of course, there may be scenarios where a weak optical sectioning capacity is actually desired, for example, to mitigate artifacts that can arise from axial sample motion. CRM maintains high resolution in this case, even over an extended focus range, since it is inherently robust against defocus aberrations.

In recent years, there have been reports of single- or few-frame enhanced-resolution imaging of conventional fluorophores based on the use image post-processing [37–39] or machine learning [40,41]. We emphasize that CRM, in its current form, does not rely on a priori knowledge about the

sample, though it may benefit from the aid of such techniques in future implementations. Additionally, one could envisage reducing the number of detection channels either by using 3-element detectors or true non-pixelated centroid detectors, further streamlining the CRM hardware. In conclusion, because of its simplicity and broad applicability, we believe CRM will be of general interest to the biological imaging community.

## REFERENCES


1. Mouli, P. K., Twig, G. & Shirihai, O. S. Frequency and Selectivity of Mitochondrial Fusion Are Key to Its Quality Maintenance Function. *Biophys. J.* **96**, 3509–3518 (2009).
2. Twig, G. *et al.* Fission and selective fusion govern mitochondrial segregation and elimination by autophagy. *EMBO J.* **27**, 433–446 (2008).
3. Hirokawa, N., Noda, Y., Tanaka, Y. & Niwa, S. Kinesin superfamily motor proteins and intracellular transport. *Nat. Rev. Mol. Cell Biol.* **10**, 682–696 (2009).
4. Maday, S., Twelvetrees, A. E., Moughamian, A. J. & Holzbaur, E. L. F. Axonal Transport: Cargo-Specific Mechanisms of Motility and Regulation. *Neuron* **84**, 292–309 (2014).
5. Kasai, H., Fukuda, M., Watanabe, S., Hayashi-Takagi, A. & Noguchi, J. Structural dynamics of dendritic spines in memory and cognition. *Trends Neurosci.* **33**, 121–129 (2010).
6. Nägerl, U. V., Willig, K. I., Hein, B., Hell, S. W. & Bonhoeffer, T. Live-cell imaging of dendritic spines by STED microscopy. *Proc. Natl. Acad. Sci.* **105**, 18982–18987 (2008).
7. Small, J. V., Stradal, T., Vignal, E. & Rottner, K. The lamellipodium: where motility begins. *Trends Cell Biol.* **12**, 112–120 (2002).
8. Barbieri, J. T., Riese, M. J. & Aktories, K. Bacterial Toxins That Modify The Actin Cytoskeleton. *Annu. Rev. Cell Dev. Biol.* **18**, 315–344 (2002).
9. Schermelleh, L. *et al.* Super-resolution microscopy demystified. *Nat. Cell Biol.* **21**, 72–84 (2019).
10. Hofmann, M., Eggeling, C., Jakobs, S. & Hell, S. W. Breaking the diffraction barrier in fluorescence microscopy at low light intensities by using reversibly photoswitchable proteins. *Proc. Natl. Acad. Sci. U. S. A.* **102**, 17565–17569 (2005).
11. Betzig, E. *et al.* Imaging Intracellular Fluorescent Proteins at Nanometer Resolution. *Science* **313**, 1642–1645 (2006).

12. Rust, M. J., Bates, M. & Zhuang, X. Sub-diffraction-limit imaging by stochastic optical reconstruction microscopy (STORM). *Nat. Methods* **3**, 793–796 (2006).
13. van de Linde, S. *et al.* Direct stochastic optical reconstruction microscopy with standard fluorescent probes. *Nat. Protoc.* **6**, 991–1009 (2011).
14. Sharonov, A. & Hochstrasser, R. M. Wide-field subdiffraction imaging by accumulated binding of diffusing probes. *Proc. Natl. Acad. Sci.* **103**, 18911–18916 (2006).
15. Jungmann, R. *et al.* Single-Molecule Kinetics and Super-Resolution Microscopy by Fluorescence Imaging of Transient Binding on DNA Origami. *Nano Lett.* **10**, 4756–4761 (2010).
16. Dertinger, T., Colyer, R., Iyer, G., Weiss, S. & Enderlein, J. Fast, background-free, 3D super-resolution optical fluctuation imaging (SOFI). *Proc. Natl. Acad. Sci.* **106**, 22287–22292 (2009).
17. Balzarotti, F. *et al.* Nanometer resolution imaging and tracking of fluorescent molecules with minimal photon fluxes. *Science* **355**, 606–612 (2017).
18. Hell, S. W. & Wichmann, J. Breaking the diffraction resolution limit by stimulated emission: stimulated-emission-depletion fluorescence microscopy. *Opt. Lett.* **19**, 780–782 (1994).
19. Gustafsson, M. G. L. Surpassing the lateral resolution limit by a factor of two using structured illumination microscopy. *J. Microsc.* **198**, 82–87 (2000).
20. Heintzmann, R. & Huser, T. Super-Resolution Structured Illumination Microscopy. *Chem. Rev.* **117**, 13890–13908 (2017).
21. Mangeat, T. *et al.* Super-resolved live-cell imaging using random illumination microscopy. *Cell Rep. Methods* **1**, 100009 (2021).
22. Sheppard, C. J. R. Super-resolution in confocal imaging. *Optik* **80**, 53–54 (1988).

23. Müller, C. B. & Enderlein, J. Image Scanning Microscopy. *Phys. Rev. Lett.* **104**, 198101 (2010).

24. Huff, J. The Airyscan detector from ZEISS: confocal imaging with improved signal-to-noise ratio and super-resolution. *Nat. Methods* **12**, i–ii (2015).

25. Roth, S., Sheppard, C. J., Wicker, K. & Heintzmann, R. Optical photon reassignment microscopy (OPRA). *Opt. Nanoscopy* **2**, 5 (2013).

26. De Luca, G. M. R. *et al.* Re-scan confocal microscopy: scanning twice for better resolution. *Biomed. Opt. Express* **4**, 2644 (2013).

27. York, A. G. *et al.* Instant super-resolution imaging in live cells and embryos via analog image processing. *Nat. Methods* **10**, 1122–1126 (2013).

28. Azuma, T. & Kei, T. Super-resolution spinning-disk confocal microscopy using optical photon reassignment. *Opt. Express* **23**, 15003–15011 (2015).

29. Tortarolo, G. *et al.* Focus image scanning microscopy for sharp and gentle super-resolved microscopy. *Nat. Commun.* **13**, 7723 (2022).

30. Zunino, A. *et al.* Open-source tools enable accessible and advanced image scanning microscopy data analysis. *Nat. Photonics* **17**, 457–458 (2023).

31. Buttafava, M. *et al.* SPAD-based asynchronous-readout array detectors for image-scanning microscopy. *Optica* **7**, 755–765 (2020).

32. Radmacher, N. *et al.* Doubling the resolution of fluorescence-lifetime single-molecule localization microscopy with image scanning microscopy. *Nat. Photonics* **18**, 1059–1066 (2024).

33. Zunino, A. *et al.* Structured detection for simultaneous super-resolution and optical sectioning in laser scanning microscopy. *Nat. Photonics* 1–10 (2025) doi:10.1038/s41566-025-01695-0.

34. Sheppard, C. J. R. & Wilson, T. Reciprocity and equivalence in scanning microscopes. *JOSA A* **3**, 755–756 (1986).

35. Castello, M., Sheppard, C. J. R., Diaspro, A. & Vicidomini, G. Image scanning microscopy with a quadrant detector. *Opt. Lett.* **40**, 5355–5358 (2015).

36. Nieuwenhuizen, R. P. J. *et al.* Measuring image resolution in optical nanoscopy. *Nat. Methods* **10**, 557–562 (2013).

37. Gustafsson, N. *et al.* Fast live-cell conventional fluorophore nanoscopy with ImageJ through super-resolution radial fluctuations. *Nat. Commun.* **7**, 12471 (2016).

38. Torres-García, E. *et al.* Extending resolution within a single imaging frame. *Nat. Commun.* **13**, 7452 (2022).

39. Zhao, B. & Mertz, J. Resolution enhancement with deblurring by pixel reassignment. *Adv. Photonics* **5**, 066004 (2023).

40. Qiao, C. *et al.* Evaluation and development of deep neural networks for image super-resolution in optical microscopy. *Nat. Methods* **18**, 194–202 (2021).

41. Chen, R. *et al.* Single-frame deep-learning super-resolution microscopy for intracellular dynamics imaging. *Nat. Commun.* **14**, 2854 (2023).

# FIGURES

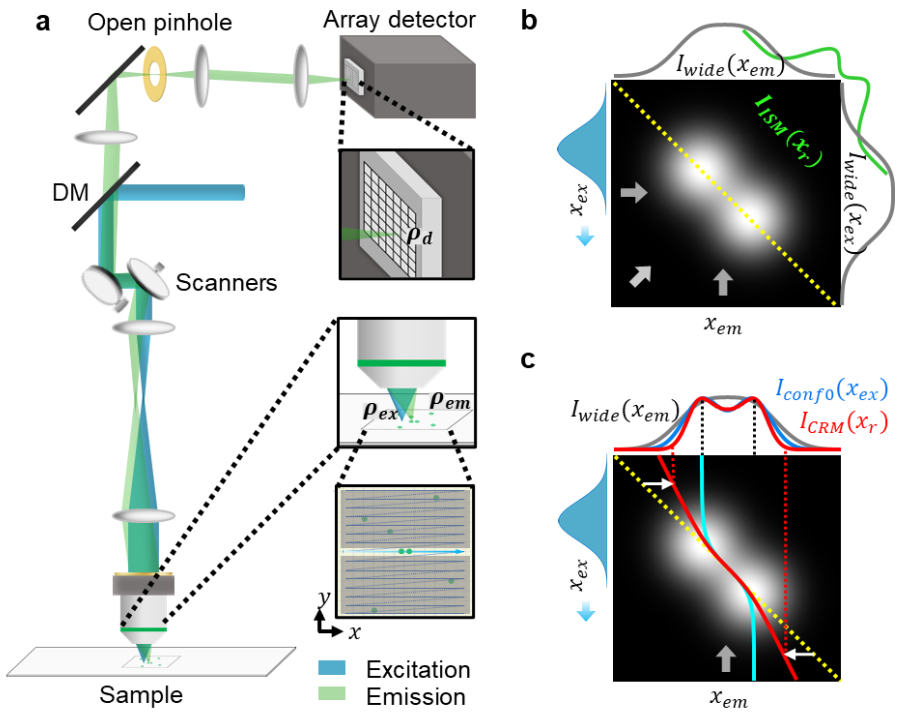


**Fig. 1| Principles of scanning microscope variations**.

**a.** General schematic -- bottom inset shows example single line of 2D raster scan spanning pair of fluorophores located at same $y$ coordinate. **b, c.** Simulations of resulting $I(x_{ex}, x_{em})$. Excitation and emission PSFs are assumed Gaussian and of equal size (blue-filled Gaussian indicates scanning excitation). In this example, fluorophore separation is half the PSF size. **b.** Horizontal and vertical projections of $I(x_{ex}, x_{em})$ (along gray arrows) lead to equivalent widefield images. An anti-diagonal projection (along green arrow) leads to an ISM image with improved resolution. Note that the image obtained from an ideal confocal microscope (closed pinhole) would be similar to the ISM image, except much weaker. **c.** CRM principle: the array detector is replaced with a centroid detector, and for every excitation scan location $x_{ex}$, the total detected intensity is reassigned (white arrows) to a location $x_r$ (red curve) situated between $x_{ex}$ and the emission centroid $\hat{x}_{em}$ (cyan curve). Normalized profiles from widefield (gray), ideal confocal (blue), and CRM (red) images are shown above.

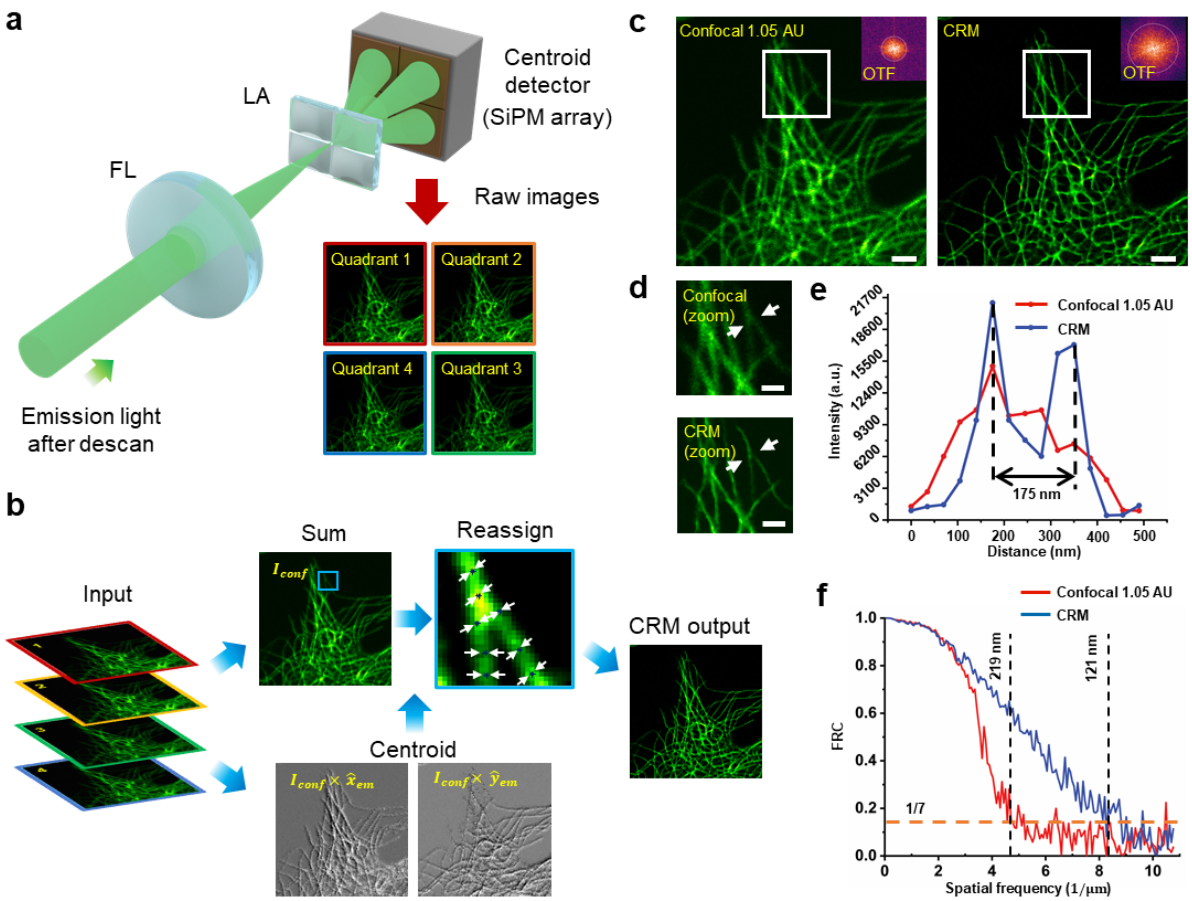


**Fig. 2 | CRM image formation with a centroid detector**.

**a.** Emission light through a moderately open pinhole (1.05 AU, not shown) is focused onto a lenslet array (LA) and detected by a quadrant SiPM array. The quadrants obtain 4 raw images upon scanning, which serve as inputs to the CRM processing pipeline. **b.** For each excitation scan position $\boldsymbol{\rho}_{ex}$, the emission total intensity $I_{conf}$ and centroid location $\hat{\boldsymbol{\rho}}_{em} = \{\hat{x}_{em}, \hat{y}_{em}\}$ are calculated from the raw images and used to perform CRM (more details in Methods). **c.** Anti-α-tubulin labeled microtubules in the fixed BPAE cell imaged by standard confocal (left, summed quadrants) and CRM (right). Insets depict spatial frequencies (log scale). Scale bar: 1 μm. **d.** Zoomed areas from white boxes in **c**. Scale bar: 500 nm. **e.** Intensity profiles across spans indicated by the white arrows in **d**. **f.** FRC analysis of standard confocal (red) and CRM (blue). Orange dashed line indicates the conventional FRC threshold used to define resolution. Experiments were repeated three times independently, with similar results.

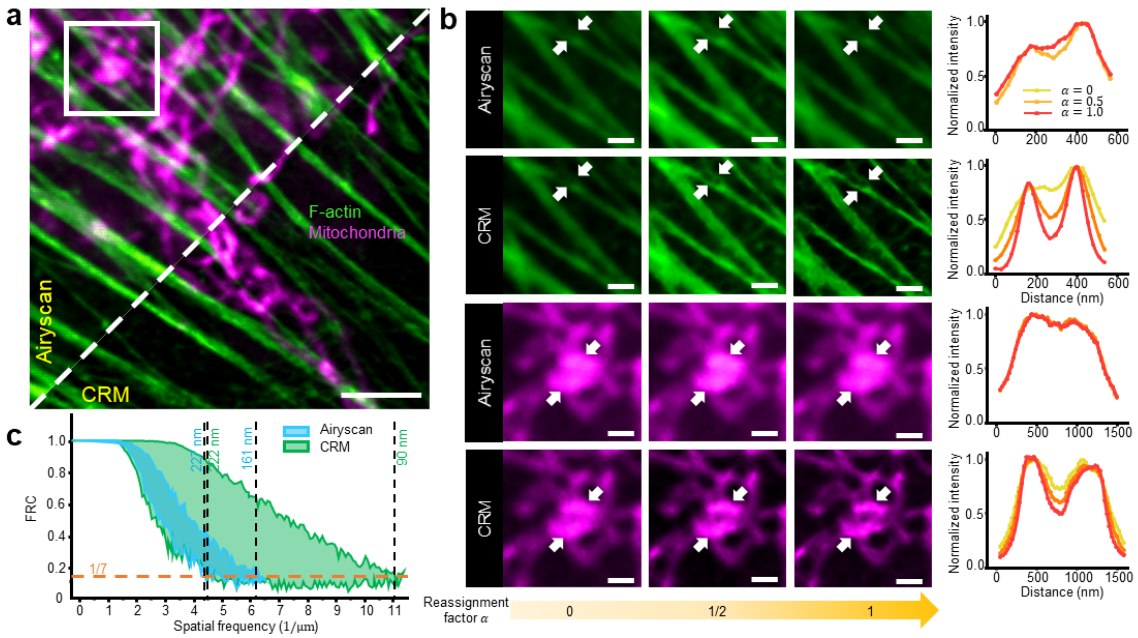


**Fig. 3 | Comparison of effect of reassignment factor on two-color CRM and ISM (Zeiss LSM 980 Airyscan2) resolution**.

**a.** Two-color images (obtained sequentially) of Alexa Fluor 488 phalloidin-labeled F-actin and MitoTracker Red CMXRos-labeled mitochondria in fixed BPAE cell imaged by Airyscan (left, detection area 1.25 AU) and CRM (right, pinhole 1.05 AU). Scale bar: 3 μm. **b.** Zoomed region (white box) obtained with different reassignment factors ($\alpha = 0, 1/2, 1$). Intensity profiles across spans indicated by the white arrows are color-coded according to $\alpha$. Note: Image sharpness increases with $\alpha$ for CRM, whereas it is maximum when $\alpha \approx 1/2$ for ISM. Scale bar: 800 nm. **c.** Spatial resolution inferred from FRC analysis in F-actin images, as a function of reassignment factors ranging from 0 to 1. Orange dashed line indicates the conventional FRC threshold used to define resolution. Experiments were repeated three times independently with similar results.

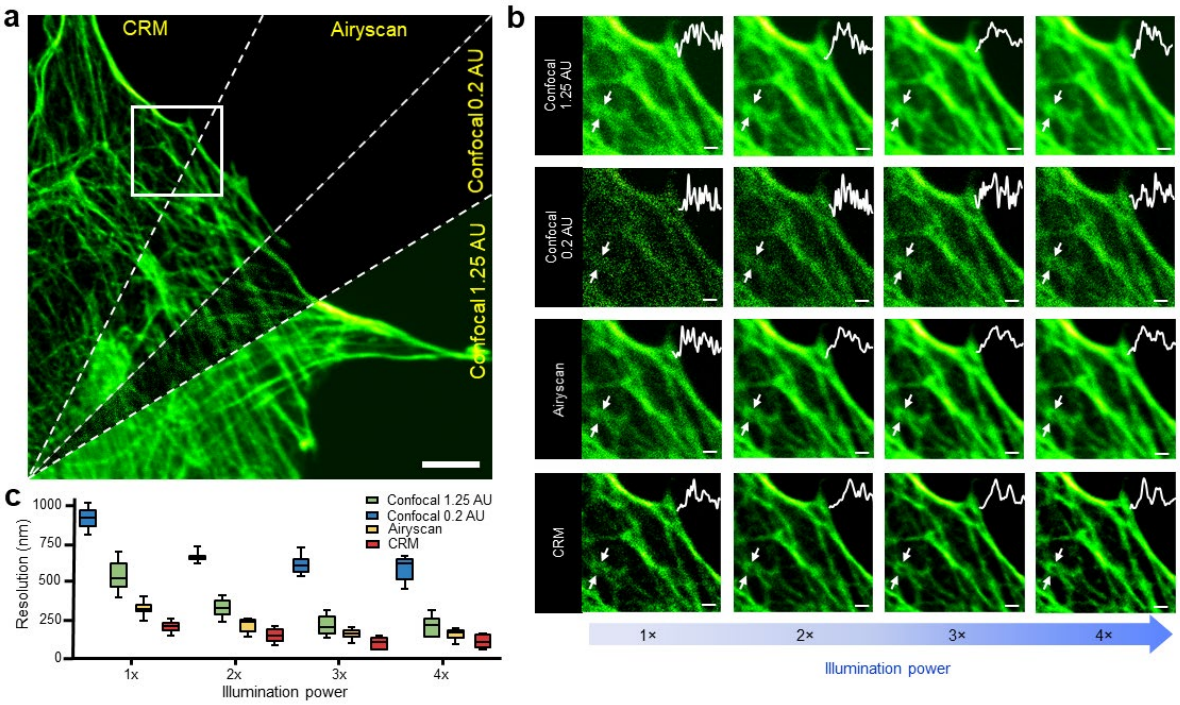


**Fig. 4 | Demonstration of CRM resolution enhancement and robustness to noise**.

**a.** Comparison of images of BPAE F-actin labeled with Alexa 488 phalloidin obtained from CRM and Airyscan. Counterclockwise from bottom: Airyscan sum mode (confocal 1.25 AU), Airyscan center channel only (confocal 0.2 AU), Airyscan SR mode (without deconvolution), and CRM (pinhole 1.05 AU). Scale bar: 3 μm. **b.** Zoomed area from the white box in **a** obtained with increasing illumination power (1× corresponds to 1.25 μW at sample, obtaining resolutions CRM: 206 nm ± 39 nm; Airyscan: 327 nm ± 44 nm; Confocal 1.25 AU: 541 nm ± 104 nm, and Confocal 0.2 AU: 908 nm ± 65 nm). Insets at top right of each panel show normalized intensity profiles across spans indicated by the white arrows. Scale bar: 500 nm. **c.** FRC analysis-based resolution statistics averaged over 8 distinct ROIs in **a**. Experiments were repeated three times independently, with similar results.

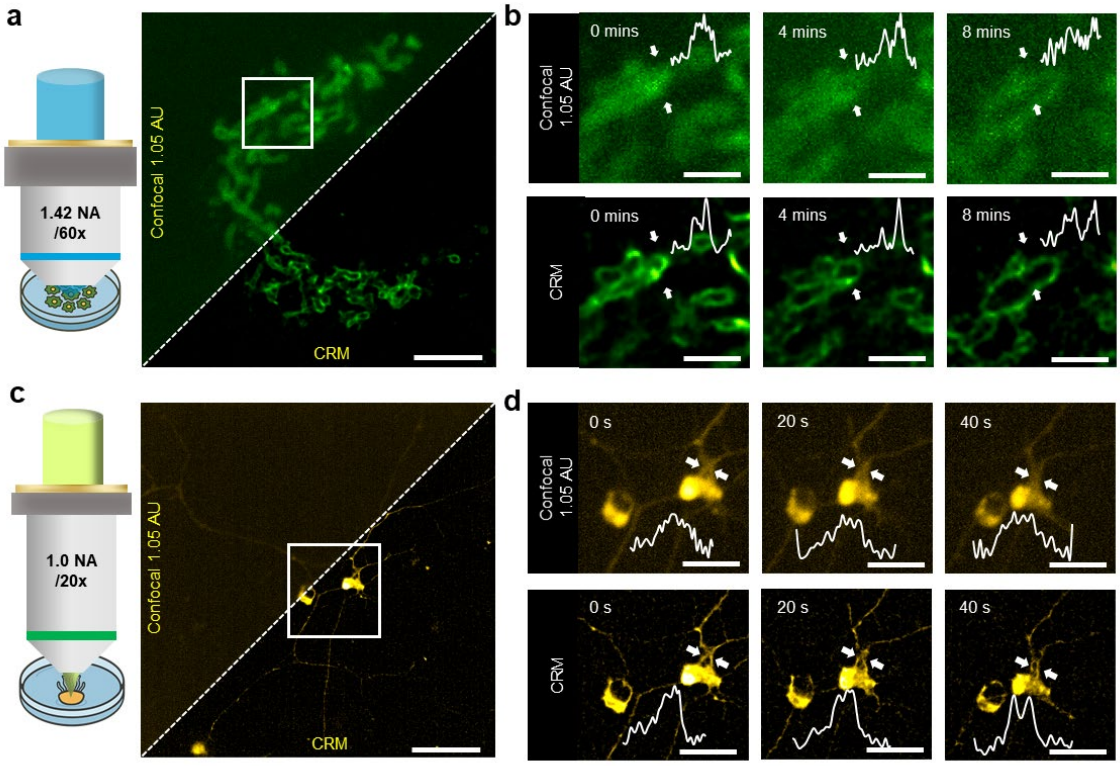


**Fig. 5 | Live-sample imaging with CRM**.

**a.** Mitochondrial dynamics in live U2OS osteosarcoma cell expressing an EGFP-tagged mitochondrial outer membrane protein (TOM20-EGFP). FOV: 16µm × 16µm. Scale bar: 3 µm. Full video shown in Supplementary Video 1. Conventional confocal image (pinhole 1.05 AU) obtained by summing of raw quadrant images. **b.** Time lapse of mitochondrial fusion from zoomed region (white box in **a**). Normalized intensity profiles across spans indicated by white arrows. Scale bar 1 µm. Full video shown in Supplementary Video 2. **c.** mCherry-expressing RFamide neuron dynamics in live jellyfish (*Clytia hemisphaerica*). FoV: 49µm × 49µm. Scale bar: 11 µm. Full video is shown in Supplementary Video 5. **d.** Time-lapse of neuron bodies and neural processes from zoomed region (white box in **c**). Normalized intensity profiles across spans indicated by white arrows. Scale bar: 4 µm. Full video is shown in Supplementary Video 6.

## ACKNOWLEDGEMENTS

We thank Zahid Yaqoob for the loan of the 1.42NA/60× objective lens, Yifei Lu for assistance with the Airyscan experiments, Francisco Sanchez and Ruifeng Hu for their assistance with sample preservation, Tianyu Wang for a helpful discussion on data acquisition system design, and Tianyu Wang and Lei Tian for initial discussions on theory. This work was partially supported by the National Science Foundation under a NSF cooperative agreement (EEC-1647837) and the National Institutes of Health (R01NS116139, R01EB029171).

## AUTHOR INFORMATION

J.Z. current address: School of Biomedical Engineering, University of Oklahoma, Norman, OK 73019, USA

### Contributions

J.M. and C.L. conceived the projects. C.L. designed and built the system. C.L. wrote and developed the reconstruction algorithm with discussion from B.Z. and Y.L.. Q.L., J.O.K., and J.Z. prepared experimental samples. C.L. performed imaging experiments with assistance from Q.L. and J.O.K.. C.L. processed the data. C.L., Q.L., J.K., B.Z., and Y.L. analyzed data. C.L. and J.M. performed simulations. C.L. and J.M. wrote the paper. All authors reviewed the manuscript. J.M., J.T.N., B.W., and T.B. supervised the project.

## COMPETING INTERESTS

J.M., C.L., and B.Z. have filed a technology disclosure with Boston University related to the CRM method described in this manuscript.

## ADDITIONAL INFORMATION

Supplementary Information is available for this paper.

Correspondence and requests for materials should be addressed to C.L. (e-mail: chuanli1@bu.edu) and J.M. (e-mail: jmertz@bu.edu).